ROYAL SOCIETY
OF CHEMISTRY

PAPER

Check for updates

Quantum 3D thermal imaging at the micro–nanoscale†

Jun Yang, [ID] *[a] Ben Q. Li,[b] Rongheng Li[b] and Xuesong Mei[c]

Real-time and accurate measurement of three-dimensional (3D) temperature field gradient maps of cells and tissues would provide an effective experimental method for analyzing the coupled correlation between metabolism and heat, as well as exploring the thermodynamic properties of nanoparticles under complex environments. In this work, a new principle of quantum 3D thermal imaging is proposed. The photoluminescence principle of quantum dots is expounded and CdTe QDs are prepared by aqueous phase synthesis. Fluorescence spectral characteristics of QDs at different temperatures are studied. The optimized algorithm of the optical spot double helix point spread function is proposed to improve the imaging, where optimized light energy increased by 27.36%. The design scheme of a quantum 3D thermal imaging system is presented. The measurement range is (−8 mm, +8 mm). The temperature is calculated according to the temperature–heat curve of quantum dots. The double helix point spread function has converted the defocus distance of QDs into the rotation angle of the double optical spot, thereby determining its position. The experimental results reveal that real-time 3D tracking and temperature measurements of quantum dots at the micro–nanoscale are achieved. Overall, the proposed nanoscale 3D quantum thermal imaging system with high-resolution may provide a new research direction and exploration of many frontier fields.

1. Introduction

The realization of three-dimensional (3D) temperature distribution measurement at the micro–nanoscale would provide more advanced research methods and suitable technologies for biological based fields to clarify the relationship between life activities of cells and heat. In turn, a study of the relationship between heat and metabolism of life would facilitate the control over progress of life activities through suitable generation of heat, providing a new theoretical basis for the accurate diagnosis of tumors at an early stage and helping the discovery of new drugs. Therefore, research on 3D thermal imaging at the micro–nanoscale has a profound theoretical significance and promising application prospects.

Since the invention of the earliest thermometers in the early 17th century, dozens of methods dealing with temperature measurement have been developed and tested. Currently,

though various methods for temperature measurement are continuously emerging, most of them focus on macroscopic objects. No detailed reports dealing with measurement methods of 3D temperature distribution at the micro–nanoscale have so far been published. However, this does not indicate the unimportance of this research field. By contrast, these measurements if successful could provide new research ideas and tools for many vital fields. For instance, the essence of metabolism is composed of a sequence of biochemical reactions with each involving thermal effects. In other words, biological cells are always reacting in the body and constantly generating energy and heat effects. Therefore, the intracellular environment is complex with various functions, resulting in gradients in internal temperature. For example, mitochondria are the main organelles for cell energy supply with relatively high ambient temperature.[1] The lesion of cells would lead to changes in their internal temperature fields. The accurate measurements of the cells and subcellular temperature would improve the detection of tumors and local inflammation, as well as provide more accurate monitoring of hyperthermia.

Quantum dots are nanocrystals with many application fields, including quantum dot displays,[2] quantum dot light-emitting diodes,[3] and quantum dot biomarkers.[4–7] For instance, Ag2S quantum dots (QDs) are employed in the second near-infrared window (NIR-II, 1.0–1.4 m) for *in vivo* dynamic tracking of human mesenchymal stem cells (hMSCs)

[a]State Key Laboratory for Manufacturing Systems Engineering, Xi'an Jiaotong University, Xi'an, 710049, China. E-mail: softyj@xjtu.edu.cn, softyj@163.com
[b]Department of Mechanical Engineering, College of Engineering and Computer Science, University of Michigan, MI 48128, USA
[c]Shaanxi Key Laboratory of Intelligent Robots, Xi'an Jiaotong University, Xi'an, 710049, China

with high sensitivity and superior spatial/temporal resolution.[8] Wei *et al.* reported a new type of DNA-templated heterobivalent QD nanoprobe able to target and image two spatially isolated cancer markers (nucleolin and mRNA) present on the cell surface or cell cytosol.[9] Ma *et al.* described a strategy for live cell imaging of single genomic loci by combining transcription activator-like effectors (TALEs) with a quantum dot labelling technique.[10]

The photoluminescence of quantum dots is closely related to temperature. Therefore, quantum dots have been applied as nanoscale temperature measuring materials in many fields,[11,12] including life science. Chen *et al.* reported a convenient and real-time assay of alkaline phosphatase (ALP) in living cells based on the fluorescence quench–recovery process under physiological pH using boron-doped graphene quantum dots (BGQDs) as fluorophores.[13] Liang *et al.* successfully assembled CdTe quantum dots onto layered double hydroxide sheets using an electrostatic self-assembly technique.[14] They noticed a linear change in peak wavelength and fluorescence intensity with temperature. Their sensors also displayed good thermal stabilities during long-term cold and heat cycles. Pugh *et al.* obtained linear relationships between the peak wavelength and temperature of CdSe/ZnS quantum dots from 295–525 K by doping CdSe/ZnS quantum dots of core–shell structure in SiO_2 with high-temperature resistant materials.[15] They also achieved a wide range of temperature monitoring.

In terms of temperature measurement of microelectronic components, traditional temperature sensors can hardly meet the requirements of accuracy and resolution due to the reduced size of the devices. In view of this, Choudhury *et al.* achieved partial thermal imaging of optical fluid devices using quantum dots,[16] while Li *et al.* successfully characterized joule heating of MEMS microstructures by quantum dots.[17] Sakaue *et al.* also studied the application of CdSe/ZnS quantum dots in supersonic wind tunnel temperature measurement.[18,19] They found that using nitrogen-vacancy centres in diamond nanocrystals (nanodiamonds), Kucsko *et al.* directly measured the local thermal environment at length scales as short as 200 nanometres.[20] Li *et al.* measured intracellular planar temperature by injecting CdTe quantum dots into the cells.[21]

Numerous studies succeeded in measuring the two-dimensional temperatures using quantum dots as probes. Overall, the average temperature of each cell can be measured but 3D temperature measurement at the micro–nanoscale cannot be achieved. The key to 3D thermal imaging is closely linked to how the axial localization of particles is achieved. Betzig *et al.* used fluorescent proteins to analyze the positions on the inside of cells.[22] Similar experiments have been performed by other researchers.[23,24] King *et al.* used the fluorescence effect of iridium nanoparticles to localize living cancer cells and improve the anti-interference ability of the probe.[25] Deschout *et al.* precisely determined the position of individual emitters using fluorescence microscopy.[26] Liu *et al.* reported a novel branched HCR (bHCR) circuit for efficient signal-amplified imaging of mRNA in living cells. This bHCR method may provide a useful platform for low-abundance biomarker detection and imaging in cell biology and diagnostics.[27] Ma *et al.* reported an aggregation-induced emission fluorogen (AIEgen)-based turn-on fluorescent aptasensor able to detect ultrasmall concentrations of intracellular IFN-gamma. Their simple and highly sensitive sensor platform may enable the exploration of cytokine pathways and dynamic secretion in a cellular environment.[28] However, most of these methods can only achieve two-dimensional localization and not 3D nano-positioning.

Von Diezmann *et al.* performed a comprehensive review of current particle 3D positioning theory and experimental research and pointed out the advantages and disadvantages of each technology.[29] Cang *et al.* achieved 3D positioning of nano-gold particles under dark field illumination with spatial resolution up to 210 nm using confocal microscopy.[30] Fish *et al.* improved the positioning algorithm and computational efficiency.[31] Wells *et al.* realized spatial localization tracking of single quantum dots in high-bright background environments.[32] Beaune *et al.* embedded quantum dots into giant vesicles and used fiber-optic fluorescence confocal microscopy to achieve 3D tracking.[33] Their method provides possibilities for hyperthermia treatment of tumors. Confocal microscopy measured one point at a time often yields moderate positioning efficiencies. In the measurement of space, the object required movement or scanning galvanometry should be employed to achieve point-by-point measurements.

The displacement measurement technique of the optical axis direction (Z-direction or lateral direction) has relatively matured in recent years. For example, methods based on centroid, Hough transform and gradient have all achieved precise positioning.[34] Most small axial displacement measurements have been conducted using out-of-focus imaging. Defocus imaging measurement of particle axial displacement was first proposed by Speidel *et al.* in 2003.[35] Afterwards, Zhang *et al.* performed numerous studies on matching methods of this measurement idea.[36] However, the overall light energy utilization rate remained moderate and not suitable for low light imaging.

The double helix point spread function is a special point spread function evolved from the vortex beam. The point diffusion function of the imaging system could be designed and then actively modified, and the distance from the focus could easily be correlated to other measured physical quantities to realize 3D positioning. Dupont *et al.* improved the method of original orbit tracking that could accurately track particles up to 5 nm. The capabilities of the system have been demonstrated using single virus tracing to follow the infection pathway of prototype foamy virus in living cells.[37] Gahlmann *et al.* demonstrated quantitative multicolor 3D subdiffraction imaging of structural arrangement of fluorescent protein fusions in living *Caulobacter crescentus* bacteria.[38] Thompson *et al.* applied the double helix point diffusion function to wide-field microscopy to realize high-resolution 3D tracking of mRNA.[39] By matching the refractive index of the objective lens immersion liquid to that of sample media, Carr *et al.* showed DHPSF imaging of up to 15 μm thick whole eukaryotic cell volumes in three to five imaging planes.[40] Bon combined

SELFI with conventional localization microscopy to visualize F-actin 3D filament networks and reveal spatial distribution of transcription factor OCT4 in human induced pluripotent stem cells at depths up to 50 μm inside uncleared tissue spheroids.[41]

In summary, existing temperature measurement technologies of quantum dots can only measure planar temperature in the cells and lack space tracking ability to realize 3D temperature measurements. Several studies dealing with particle localization technology have been reported but 3D thermal imaging temperature measurements in micro–nanoscale spaces have not so far been achieved. By combining the research and applications of current quantum dot temperature measurements with the double-helix point spread function, we were able to use quantum dots as temperature measurement probes to realize 3D localization of probes and achieve 3D thermal imaging of quantum dots at micro–nanoscales. This principle provided an effective experimental means not only for the accurate measurement of a 3D temperature field gradient map of the cells in real time and analysis of coupled correlation between metabolism and heat but also for exploring the kinetic characteristics of nanoparticles in complex environments. The proposed principle could further improve the accuracy and reliability of tumor diagnosis and new drug discovery.

2. Experimental section

2.1. Preparation of quantum dot temperature measurement probe

The nature, purity and source of the pharmaceutical reagents used for the synthesis of CdTe quantum dots are listed as follows. They were all used as received without further purification. Deionized water was employed for all experiments unless otherwise stated. $C_4H_6O_4S$ was purchased from Aladdin Reagent (Shanghai) Co., Ltd and is of analytical grade. Na_2TeO_3 was purchased from Tianjin Guangfu Fine Chemical Co., Ltd with analytical reagent. $CdCl_2$ was purchased from Tianjin Guangfu Fine Chemical Co., Ltd and is of analytical grade. $NaBH_4$ was purchased from Shanghai Shan Pu Chemical Co., Ltd with analytical reagent. $Na_3C_6H_5O_7$ was purchased from Tianjin East Tian Zheng Fine Chemical Reagent Co., Ltd and is of analytical grade.

2.2. Synthesis of QDs for thermal sensing

Details of the synthesis process are reported in the literature.[42] Typically, 4 ml of 0.04 mol L^{-1} $CdCl_2$ was first diluted to 50 ml with ultrapure water and placed in a three-necked flask. Next, 100 mg sodium citrate, 4 ml of 0.01 mol L^{-1} Na_2TeO_3 solution, 50 mg mercaptosuccinic acid (MSA) and 50 mg $NaBH_4$ were successively added under constant stirring. When the solution color turned yellow-green, nitrogen gas was introduced and then the flask was condensed and refluxed several times at 100 °C to obtain CdTe quantum dots with different particle sizes and fluorescence properties.

2.3. Experiment equipment used for synthesis of CdTe quantum dots

A constant temperature magnetic stirrer with specification 78HW-1 was purchased from the manufacturer Hangzhou Instrument Motor Co., Ltd. An electronic balance with specification JA-1103A was purchased from the manufacturer Shanghai Precision Science Instrument Co., Ltd.

2.4. Solution for temperature sensing test

The thermal sensitivity of the QD solution was calibrated using the experimental setup (Fig. 1d). The QDs were dispersed in phosphate buffer solution (PBS) and the sample solution was placed on a flat plate whose temperature was controlled by using a transformer. The concentration of the CdTe QDs can be estimated at 24 μM. A thermocouple was inserted into the sample solution to monitor the change in solution temperature during the experiments. The QD solution was excited by using a laser source and the emitted PL spectra from the QDs were collected and analyzed by using the spectrograph. In the optical path for emission acquisition, an optical filter was employed to filter out the excitation spectra. The spectral data were collected after the temperature reached thermal equilibrium. This way, each spectral curve was obtained for a selected temperature, producing temperature-dependent spectra for the QDs. The relationship between the peak shifts of the curves and the corresponding temperatures read from the thermocouple was then established.

2.5. Co-culture of QDs and living liver cancer cells

The liposome transfection method was employed for the QD intake, in which liposomes were used as vehicles to transfer the QDs into the cells. 50 liver cancer cells were incubated and the culture media were changed every 1–2 days. After that, a 1 mL cell suspension with 1.0×10^5 cells was sub-cultured in a 20 mm confocal Petri dish, followed by incubation for a period of 10 h. At this point, QDs with the appropriate concentration were added for loading using a Lipofectamine 2000 Reagent kit.

2.6. Verification of the optimization effect of double spiral point spread function

The Spatial Light Modulator (SLM) model was X13138-01 from Hamamatsu in Japan, a space phase modulator with reflection-type electrical addressing based on the CMOS circuit to directly control liquid crystal voltage and yield high precision phase modulation. The optimization of wavefront control design of x13138-01 also led to a high light utilization rate and elevated diffraction efficiency. This module was mainly used in aberration correction, pulse shaping, optical clamp, optical vortex generation, and other applications. The detailed parameters are listed as follows: resolution 1272×1024, CCD size 15.9 mm × 12.8 mm, pixel size 12.5 μm, filling factor 96%, and modulation wavelength range 400–700 nm.
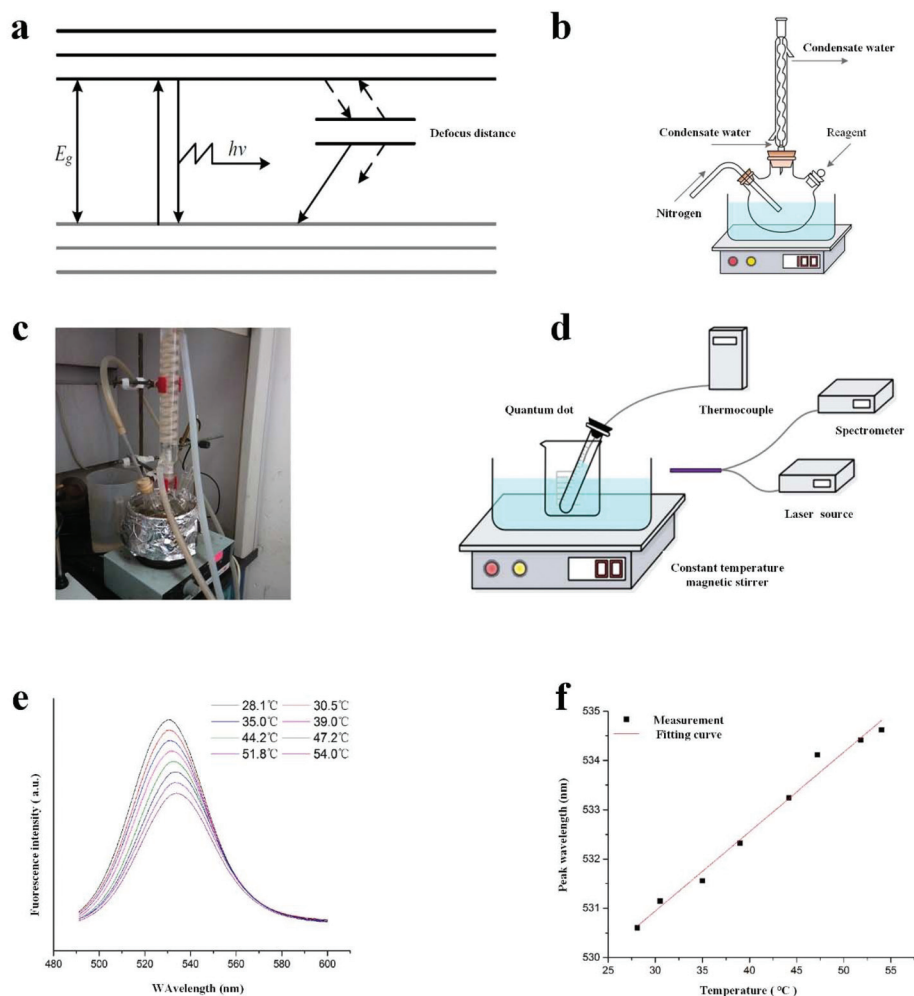
Fig. 1 Fluorescence temperature profiles of quantum dots and temperature measurements. (a) Photoluminescence principle of quantum dots. (b) Aqueous phase synthesis experimental device schematic of quantum dots, and (c) synthetic experimental device. (d) The experimental device employed for studying temperature characteristics of quantum dots. (e) Fluorescence spectra of quantum dots at different temperatures (*i.e.,* 28.1 °C, 30.5 °C, 35.0 °C, 39.0 °C, 44.2 °C, 47.2 °C, 51.8 °C, 54.0 °C), and (f) relationship between fluorescence peak wavelength and temperature.

2.7. Design of microscopic imaging system

The microscope was composed of an objective lens and eyepiece, wherein the objective lens magnifies the observed object into the real image on the focal plane of the eyepiece. The images will then pass through the eyepiece for human eye observation at infinity. The performance of the entire microscope was primarily determined by its objective lens. The conjugate distance of the objective lens, also known as the object–image distance, will refer to the basic size of the optical installation pressing the axial distance between the object surface and first image plane in air.

2.8. Design and construction of positioning and tracking system

The ③ filter consisted of an interference filter GCC-202003 from Daheng Optoelectronics. The center wavelength of the filter was determined as 532 nm, and the peak wavelength transmittance was greater than 55%. The camera model was

based on iXon Ultra 888 from Andor, UK. The camera consisted of a million-resolution electron-multiplying charge-coupled device (EMCCD) camera with pixel size up to 13 μm, greatly reducing system noise by a built-in cooling module suitable for low-light detection, super-resolution micro imaging, and other applications.

3. Results and discussion

3.1. Fluorescence profiles of quantum dots and temperature measurements

Photoluminescence refers to luminescence generated by excitation of the luminescent material when exposed to light. The process of quantum dot generated fluorescence can be divided into three stages: photon absorption, energy transfer, and photon emission. Using external light as an incident source on quantum dots, the electrons present in the valence band will jump to different quasi-discrete molecular levels in the con-

duction band after absorption of photons, producing electron–hole pairs. Because the excited states of electrons are often unstable, the electrons could easily return to ground states. This leads to energy loss through radiative and non-radiative jump. A few electrons could directly jump back to the conduction band, releasing energy in the form of photons and emitting fluorescence. The fluorescence is mostly captured by electron traps and quenched in the form of non-radiation (Fig. 1a). The effect of temperature on the optical band gap of quantum dots can be described by the well-known Varshni empirical formula[43,44] (ESI†).

The main purpose of this paper was to achieve temperature measurement through the relationship between fluorescence spectroscopy of quantum dots and temperature. The synthesis of CdTe quantum dots using current aqueous phase synthesis was relatively straightforward. The fluorescence yield could meet the experimental requirements. Therefore, CdTe quantum dots were fabricated by the aqueous phase synthesis route and then employed as temperature measurement probes. The properties of the prepared CdTe QDs such as the size, zeta potential, surface coating, and quantum yield are 2.7 nm, −34 mV, mercaptosuccinic acid, and 70%, respectively.

Thioglycerol-coated CdTe quantum dot nanomaterial aqueous solution was first prepared by T. Rajh *et al.* in 1993.[45] Afterwards, Gao *et al.* fabricated water-soluble CdTe quantum dots with good fluorescence performances using thioglycolic acid as a stabilizer and NaHTe as a Te source by the aqueous phase method.[46] However, this process was based on two-steps and the Te source could easily be oxidized, hence not convenient. Here, the improved one-step method was employed for the synthesis of quantum dots with high fluorescence yield and a convenient procedure.

The experimental device was used for the preparation of quantum dots (Fig. 1b and c). The oil bath was used to heat and keep the reactants warm. Continuous magnetic stirring was employed throughout the whole process and the magnetic rotor in a three-mouth flask was rotated sometimes to ensure sufficient mixing of the reactants.

The chemical reactions can be summarized as follows:

$$4TeO_3^{2-} + 3BH_4^- \rightarrow 4Te^{2-} + 3BO_2^- + 6H_2O$$
$$CdL + Te^{2-} \rightarrow CdTe + L \quad L\text{-}MSA \tag{1}$$
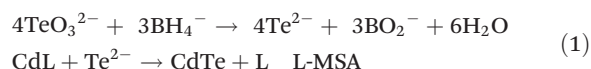
During the reaction process, excess $NaBH_4$ will reduce TeO_3^{2-} into Te^{2-} and protect it from oxidation. The newly formed Te^{2-} will then react with Cd^{2+} to generate the CdTe nucleus, which will continuously grow during condensation and reflux processes.

Here, we considered that volumes of the obtained quantum dots kept increasing as preparation prolonged. Hence, the spectral temperature characteristics of green light quantum dots with smaller volumes and strong fluorescence intensities at around 550 nm were studied using the experimental device (Fig. 1d).

This experimental device was able to achieve heating and insulation of quantum dots through a water bath. It also allowed synchronization of fluorescence excitation, acquisition by coupling the spectrometer to excitation light with an optical fiber, and simultaneous collection of temperature data of quantum dots using the thermocouple. According to the operating manual of the spectrometer, the slit was set to 200 µm and the final optical resolution to 0.39 nm.

The fluorescence spectra of quantum dots recorded at different temperatures are compared (Fig. 1e). The temperature of quantum dots increased and the fluorescence spectrum shifted to longer wavelengths. This pattern was consistent with the previous theoretical analysis, showing that the increase in temperature declined both the optical band gap of quantum dots and their fluorescence photon energies. These features increased the wavelength of fluorescent light.

The fluorescence spectra of quantum dots at different temperatures were fitted by Gaussian fitting to yield peak wavelengths (Table 1). The data were then fitted to obtain the fitting line (Fig. 1f). The fitting line can be expressed by eqn (2):

$$\lambda = 0.16T + 526.10 \tag{2}$$

where: λ presents the fluorescence peak wavelength of quantum dots in nm and T is the temperature of quantum dots in °C.

Analysis of the data revealed that the wavelength of quantum dot fluorescence peaks increased as temperature increased, consistent with the theoretical analyses. The peak wavelength temperature sensitivity of the quantum dots was estimated to be 0.16 nm °C^{-1}. At a spectral resolution of 0.1 nm, the temperature measurement resolution was recorded as 0.625 °C, suitable for most applications.

3.2. 3D tracking principle of quantum dots

To achieve 3D temperature measurement at the micro–nano scale, 3D localization and tracking of the probe are important factors to consider. In particular, the axial localization of the particles is critical in achieving better results. The optimal design of the double-helix point spread function was conducted based on the existing literature to improve the defocusing imaging effect of the double spot.

The distribution of the image field of surface using both theoretical calculation and actual collection at a point light source located at the focal plane of the object is illustrated

Table 1 Fluorescence peak wavelength of quantum dots at different temperatures

Temperature (°C)	Peak wavelength (nm)
28.1	530.60
30.5	531.14
35.0	531.56
39.0	532.32
44.2	533.24
47.2	534.11
51.8	534.41
54.0	534.62

(Fig. 2a and b). At this time, in addition to the two main spots on the image surface, a more obvious side lobe appeared with connection between the main light clusters.

If both effects can be alleviated or eliminated by improving the phase modulation function, the imaging efficiency of the system will be enhanced and image processing in latter quantum dot locations will be facilitated.

Here, an algorithm was designed to optimize the modulation function based on the linear characteristics of the 4f system. The purpose was to reduce the influence of stray light on the algorithm as much as possible without affecting defocusing double-helix characteristics. The overall idea of the algorithm was based on iterative optimization (Fig. 2c).

To ensure that defocusing double helix characteristics of the imaging system were not affected after optimization, the algorithm required a selection of enough defocus planes for iterative optimization. Here, a total of 9 defocusing planes

with defocusing distances of 0 mm, ±2 mm, ±4 mm, ±6 mm and ±8 mm were selected as optimization objects.

Before optimizing the algorithm, it would be necessary to first calculate the imaging corresponding to each defocusing distance when using the pure phase modulation function. Also, the spot portion should be maintained and normalized as expected images.

When the point light source was located on the focal plane of the object, the above steps led to results (Fig. 2d and e). The theoretical image of the point optical source at the focal plane of the object is presented (Fig. 2d) and the expected image is obtained after processing (Fig. 2e). The image retained only the main spot and all other light was removed.

In the algorithm, the pure phase modulation function was taken as the initial modulation function. The defocusing imaging corresponding to each defocusing surface was then calculated each time and subtracted from expected imaging to
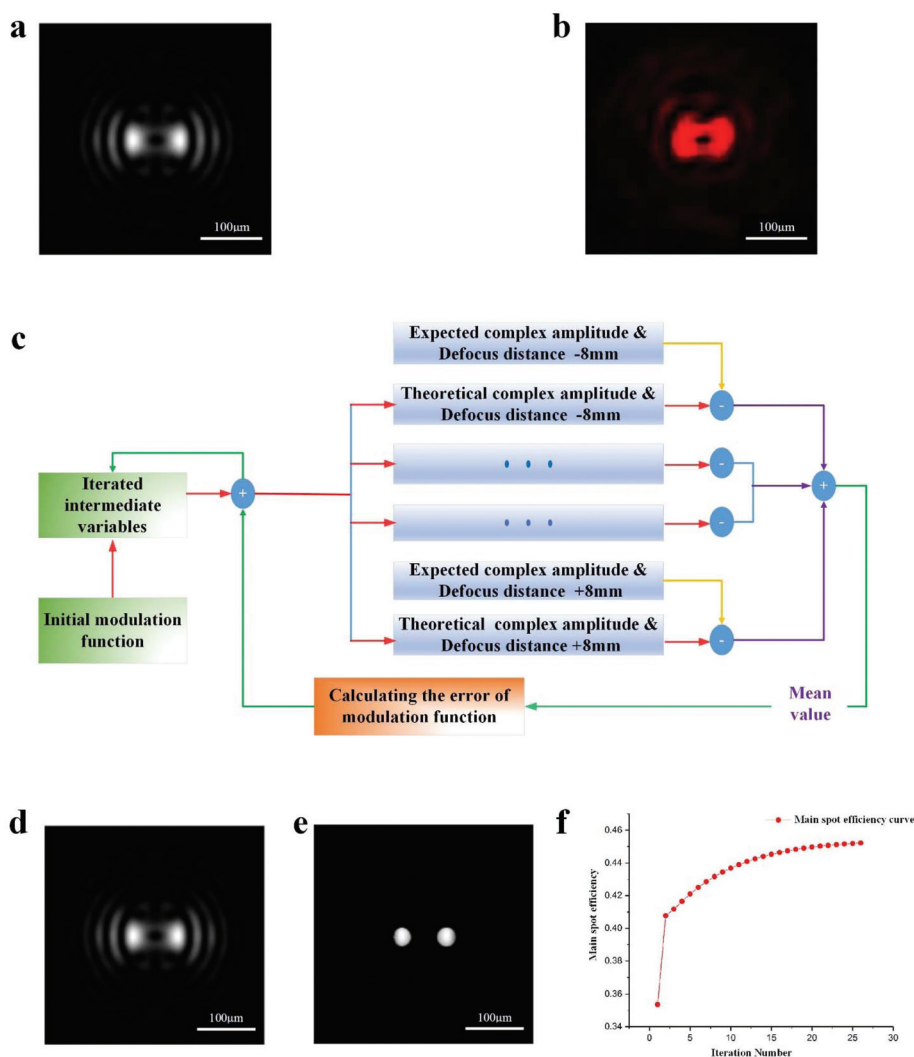

Fig. 2 Design of the optimized algorithm of the double-helix point spread function. (a) Theoretical images at the point optical source located on the focal plane of the object, and (b) measured imaging. (c) Optimized algorithm process. (d) Theoretical images of the point optical source at the focal plane, and (e) expected imaging. (f) Variation of efficiency of the main spot during optimization.

obtain the deviation between both. The deviation between each defocus surface and expected deviation was then averaged, and deviation corresponding to the modulation function was obtained by reversed operation. The latter was added to the modulation function obtained during previous iteration and served as the modulation function of next iteration.

After each iteration, the algorithm was set to solve the average efficiency of the main spot, representing the ratio of main spot energy to total imaging energy. The data were then compared to those of previous iteration. If the efficiency

tended to converge, the iteration was ended. The efficiency of the main spot increased greatly during the first iteration followed by a steady increase until reaching a stable value (Fig. 2f). At the 26th iteration, the efficiency converged and the algorithm ended. At this time, the efficiency of the main spot was recorded as 45.22%. This value was 27.88% higher than that of the initial input.

The obtained modulation function at the end of iteration is presented (Fig. 3a and b), the amplitude modulation part without attenuated light in the range of clear aperture (Fig. 3a)
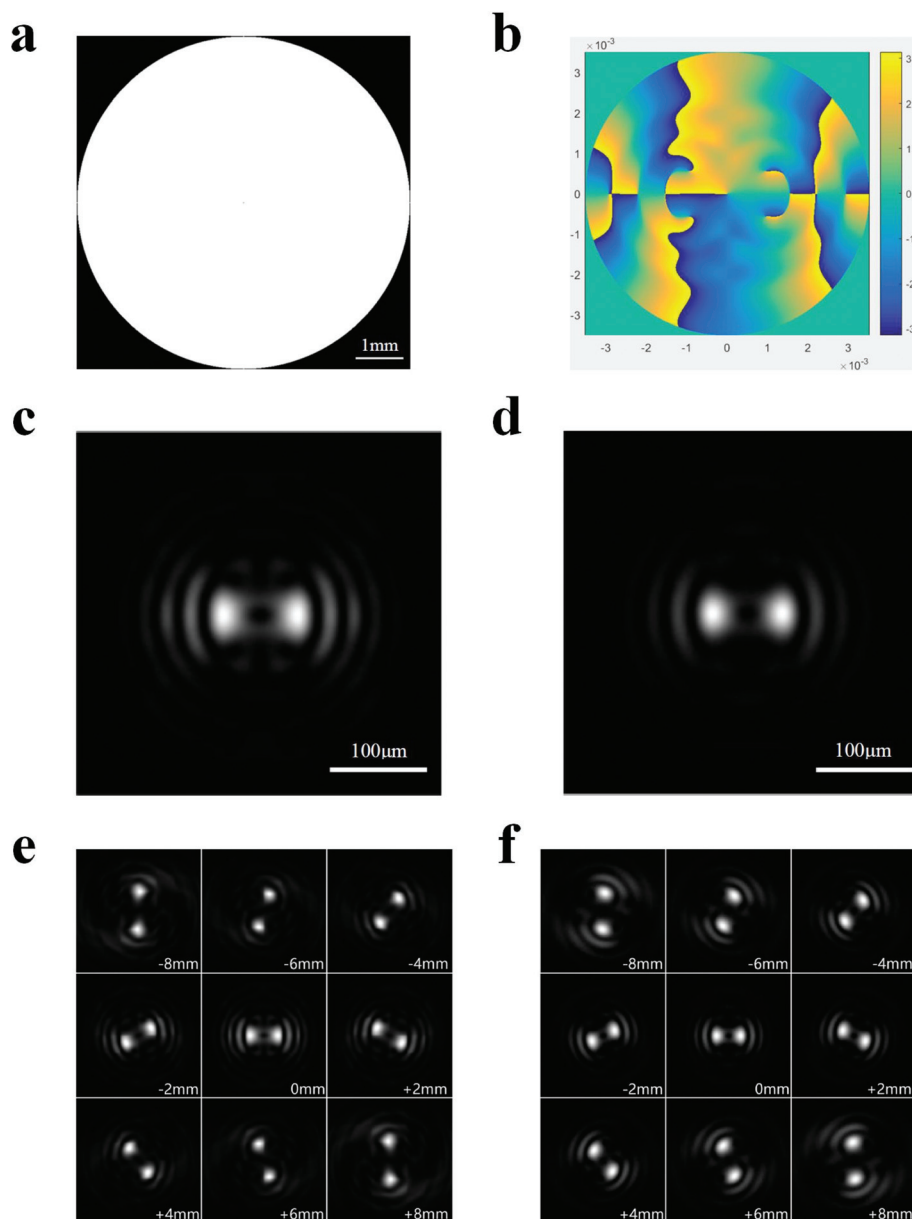

Fig. 3 Imaging schematic diagram of double light spot before and after optimization of the double helix point spread function. (a) Optimized modulation function with amplitude modulation. (b) Optimized modulation function with phase modulation. (c) Theoretical imaging effects before modulation function optimization, and (d) after optimization. (e) Imaging effect of each defocusing surface before optimization (i.e., a total of 9 defocusing planes with defocusing distances of 0 mm, ±2 mm, ±4 mm, ±6 mm and ±8 mm were selected as optimization objects), and (f) after optimization.

and (Fig. 3b) as the phase modulation effect of the phase delay effect of the modulation function on light.

The imaging effect of the system on the point light source located on the focal plane of the object compared to the modulation function before and after optimization is illustrated (Fig. 3c and d). The imaging by the modulation function before optimization is presented in Fig. 3c and imaging by the modulation function after optimization in Fig. 3d.

Imaging by the modulation function after optimization showed significantly reduced side lobe light. The connection effect between the double spots was also significantly decreased, indicating the optimization effect of the algorithm.

The effects of the nine selected defocusing surfaces before and after optimization are compared, where Fig. 3e represents the defocusing imaging before optimization and Fig. 3e the imaging effect of the optimized modulation function.

Comparison of defocusing surface images revealed that main light spots corresponding to each defocusing surface became round after optimization, and connection between the light spots obviously weakened. Imaging with small defocus distances showed significantly weakened side lobe light and enhanced when the distance from the focus became larger. However, the overall spot efficiency increased with the optimization process.

To verify the accuracy of the optimization algorithm, the optical path in Fig. 4a was designed and tested. The spatial light modulator (SLM) was utilized to replace the phase plate. The light was then modulated and reflected onto the prism to produce images on the CCD.

The experimental light path in Fig. 4b was constructed according to Fig. 4a. The dotted line position represented the optical axis. The laser beam first passed through the ② polar-
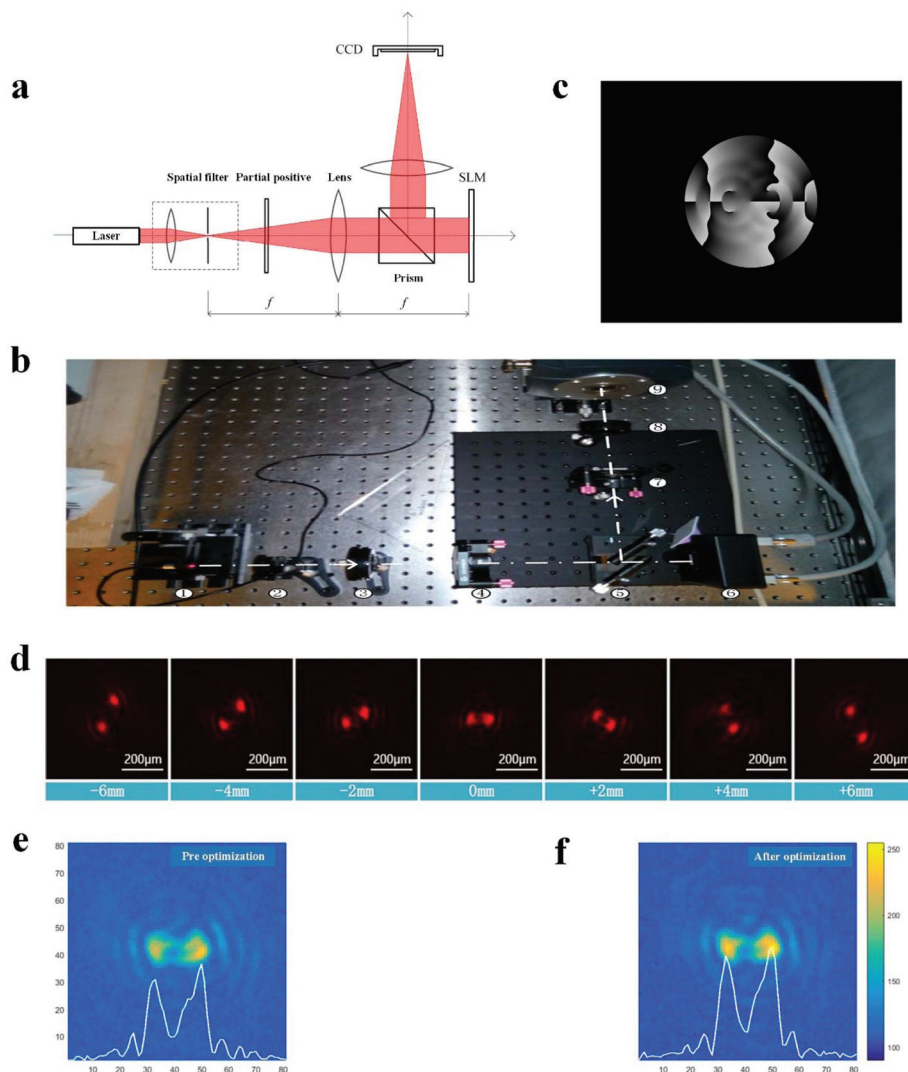

Fig. 4 Schematic diagrams for verification of the optimization effect of the double helix point spread function. (a) Design of the experimental optical path used for verifying the optimized algorithm. (b) Experimental SLM light path: ① laser, ② polaroid, ③ aperture, ④ lens, ⑤ prism, ⑥ SLM, ⑦ lens, ⑧ aperture, and ⑨ camera. (c) SLM output diagram. (d) Defocus imaging of the optimized modulation function. (e) Imaging comparison before optimization, and (f) after optimization.

oid, ③ aperture, ④ lens and ⑤ prism, and then reflected by ⑥ SLM modulation to ⑤ prisms. The resulting beam will be passed through the ⑦ lens and ⑧ aperture to finally be imaged on the ⑨ camera. The role of the ② polaroid was to attenuate the light to prevent damage to the camera. Meanwhile, this will ensure the direction of polarization of light to fit with the requirements of the modulator.

Prior to experiments, the SLM was set to work in mirror mode, and then the position of the laser was adjusted along the optical axis. Meanwhile, the camera was tested for image collection and the position was marked as zero at a small imaging spot. Subsequently, the modulation function was transformed into the corresponding gray scale diagram as the input of the SLM at a wavelength of 650 nm according to the user manual of X13138-01 (Fig. 4c).

Due to the location error of SLM installation, the laser beam would inevitably deviate from the modulation region of the SLM. Therefore, the unoptimized modulation diagram was first output to the SLM during the experiment, and deviation of the XY direction of the output diagram was fine-tuned to clarify the double helix imaging.

From −10 mm to +10 mm, the defocus distance was moved every 2 mm and the corresponding defocus image was recorded. At a constant XY direction shift, the optimized modulation diagram was set as an output to the SLM and then both defocus distance and corresponding images were recorded.

Fig. 4d shows partial collected defocusing images. The use of the optimized modulation function did not change the defocusing double-helix characteristics of the imaging system. As the point light source moved forward along the optical axis, the double spots rotated clockwise around their center.

To compare the imaging effects before and after optimization, the laser position was adjusted to ensure the point source located in zero point. The exposure time was set to 10 μs, and the images were separately collected at the modulation function before and after optimization.

Fig. 4e depicts the imaging contrast between before and after optimization. The white curve represented light intensity at each point on the line where a bright spot was located. The light intensity of the main light spot after optimization significantly improved. The energies of the main spot were then extracted and compared. The optimized light energy was 27.36% higher than that obtained before optimization. This value was also close to the theoretical 27.88%, demonstrating the successful optimization effect of the designed algorithm.

3.3. Design of quantum 3D thermal imaging system at micro–nanoscale

To achieve 3D temperature measurement at the micro–nanoscale, quantum dot spectral measurements required to be synchronized with their 3D positioning in the same system. In the previous chapter, the double-helix point diffusion function at measurements ranging from −8mm–+8 mm was achieved through simulation and experiments. To scale the measure-

ment range to the micro–nanoscale, the defocus distance of quantum dots required pre-amplification.

The measurement scheme is thus adopted to pre-amplify the measured space using a microscopic imaging system ①. The optical path of microscopic imaging was divided into two parts to enter the fluorescent temperature measurement system ③ of quantum dots and the 3D positioning system ② (Fig. 5a).

The microscopic imaging system was mainly composed of an excitation light source, carrier stage, objective lens, and spectroscopic device. The microscopic imaging system will perform fluorescence excitation on quantum dots. The images
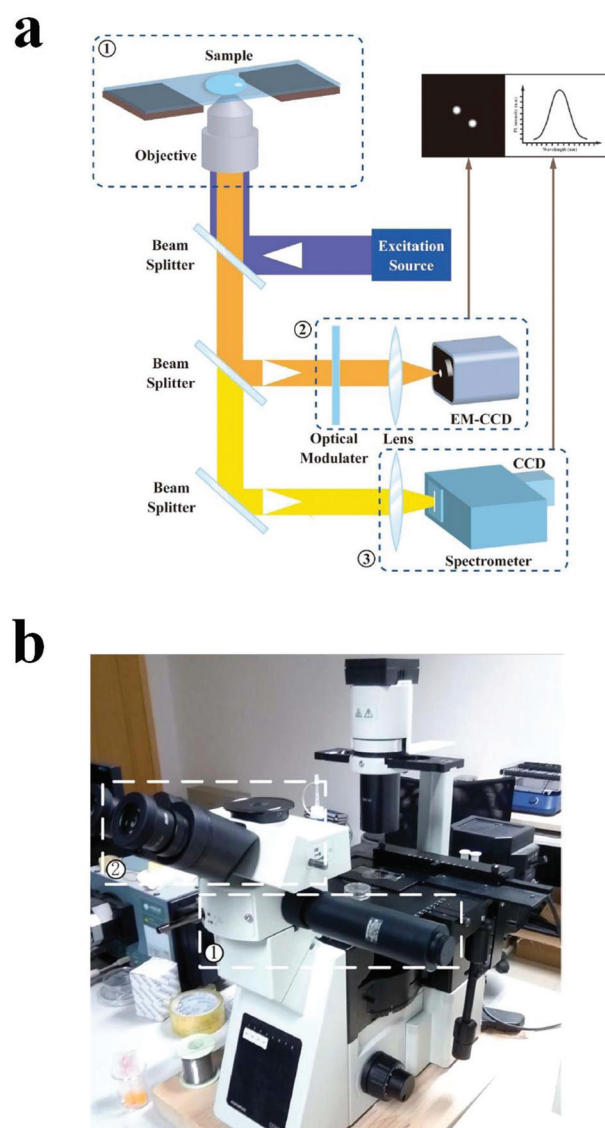

Fig. 5 Three dimensional (3D) thermal imaging system of quantum dots. (a) Schematic diagram of system design scheme: ① microscopic imaging system, ② and 3D positioning system of the quantum dots, ③ fluorescence temperature measurement system of quantum dots. (b) Installation effect of the triplex transposition interface and right transposition interface: ① right transposition interface U-DP and ② triplex transposition interface U-TR30-2.

will then be amplified by the objective lens and introduced into both the quantum dot fluorescence temperature measurement system and quantum dot 3D positioning system, respectively.

The main instrument of the quantum dot fluorescence temperature measurement system was the fluorescence spectrometer able to perform spectral measurement and analysis on fluorescence from the microscopic imaging system to obtain peak wavelength. The quantum dot temperature will then be calculated according to the thermodynamic characteristic curve of the quantum dots.

The core of the quantum dot 3D positioning system was based on the double-helix point spread function, designed to convert the defocus distance of quantum dots into the rotation angle of the double spot and then determine the relative position of the quantum dots according to the rotation angle. The amplified imaging of quantum dots by using the microscopic imaging system was located in the focal plane of the object of the location system. After magnification of quantum dots by the microscopic imaging system, the defocus distance will also be magnified at about square of lateral magnification. For example, using objective lens with a magnification of 100×, the quantum dot with a diameter of 10 nm and deviation from the focus of 1 μm was amplified to yield an image with a diameter of 1 μm and deviation from the focus image space of 10 mm.

The main function of the microscopic imaging system was fluorescence excitation of quantum dots and light splitting after image amplification. This was designed based on the existing inverted fluorescence microscope Olympus IX53.

The microscope was equipped with a spectroscopic outlet, which could directly connect to the fluorescence temperature measurement system. To connect the microscopic system with a quantum dot 3D positioning system, the right transposition interface U-DP and triplex transposition interface U-TR30-2 were configured and installed on the microscope (Fig. 5b). ① presented the right transposition interface U-DP dividing the light originally emitted from the eyepiece into two parts. The first part will be excited to enter the positioning system along the direction of the eyepiece while the other part along the interface. ② showed the triplex transposition interface U-TR30-2 used together with ① to facilitate the adjustment of field view during the experiment.

The key design of the quantum dot 3D positioning system was based on the double-helix point diffusion function, so that the imaging system can defocus the object and double helix of image space. Depending on the light modulation device, a phase plate or spatial light modulator can be used.

Compared to the spatial light modulator, the phase plate will not require the polarization of light. Moreover, the resolution of grid division can usually reach 100 nm or even smaller using micro-machining technology, much higher than that of the spatial light modulator and more suitable for low light applications. Therefore, the phase plate was selected for system design.

A phase plate was designed for wavelength at 650 nm, and its defocus double helix characteristics were verified through experiments. Using green light quantum dots with peak wavelengths around 532 nm for temperature measurement, the influence of wavelength deviation on defocus characteristics of the system could be determined.

Therefore, the MatLab program was written to calculate the imaging of the system at different defocus distances at the wavelength of light source of 532 nm, and the processed phase plate was used as the light modulation device (Fig. 6a). The system still showed the characteristics of the defocusing double helix. As the point light source moved forward along the optical axis, the double spots rotated clockwise around its center.

The rotating arc was extracted from the images and compared to data obtained at a wavelength of 650 nm (Fig. 6b). The rotating arc corresponding to 532 nm wavelength was relatively large at the same defocus distance. Hence, the axial distance measurement range of the system was relatively small and ranged from −6 mm to +6 mm.

The design and construction of the quantum dot positioning system were performed according to the experimental SLM optical path shown in Fig. 4b and the results are depicted in Fig. 6c. The dotted line represented the direction of light propagation. The beam from the microscopic imaging system passed through the ① lens, ② aperture, ③ filter, ④ phase plate, ⑤ mirror, ⑥ lens and ⑦ aperture to finally be imaged on the ⑧ camera.

According to camera photosensitive element size and microscopic objective magnification, the field view was calculated as 133 μm × 133 μm and positioning resolution of quantum dots along the XY direction was 130 nm. Since pixel size in the photosensitive element was accurate up to 1 μm and the system employed a microscopic objective at a magnification of 100, the theoretical positioning accuracy in the lateral direction was recorded as 10 nm.

The equivalent single lens system of a microscopic system was obtained as shown in Fig. 6d. The equivalent focal length f was 2.205 mm, the focus–object distance l was 22.05 μm, and focus–image distance L was 220.5 mm.

According to geometric optics, the lateral magnification $β$ could be expressed by eqn (3):

$$\beta = \frac{L}{f} = \frac{f}{l} \qquad (3)$$

where L presents the focus–image distance in m, f is the focal distance of the lens in m, and l is the focus–object distance in m.

Considering left to right as the positive direction, the offset distance of the object could be assumed as Δl. The position of its conjugate image will also be offset with an offset distance of:

$$\Delta L = \frac{f^2}{l + \Delta l} - L \qquad (4)$$

Based on eqn (4), the MatLab program was written to calculate Δl from −600 nm to +700 nm and ΔL corresponding to
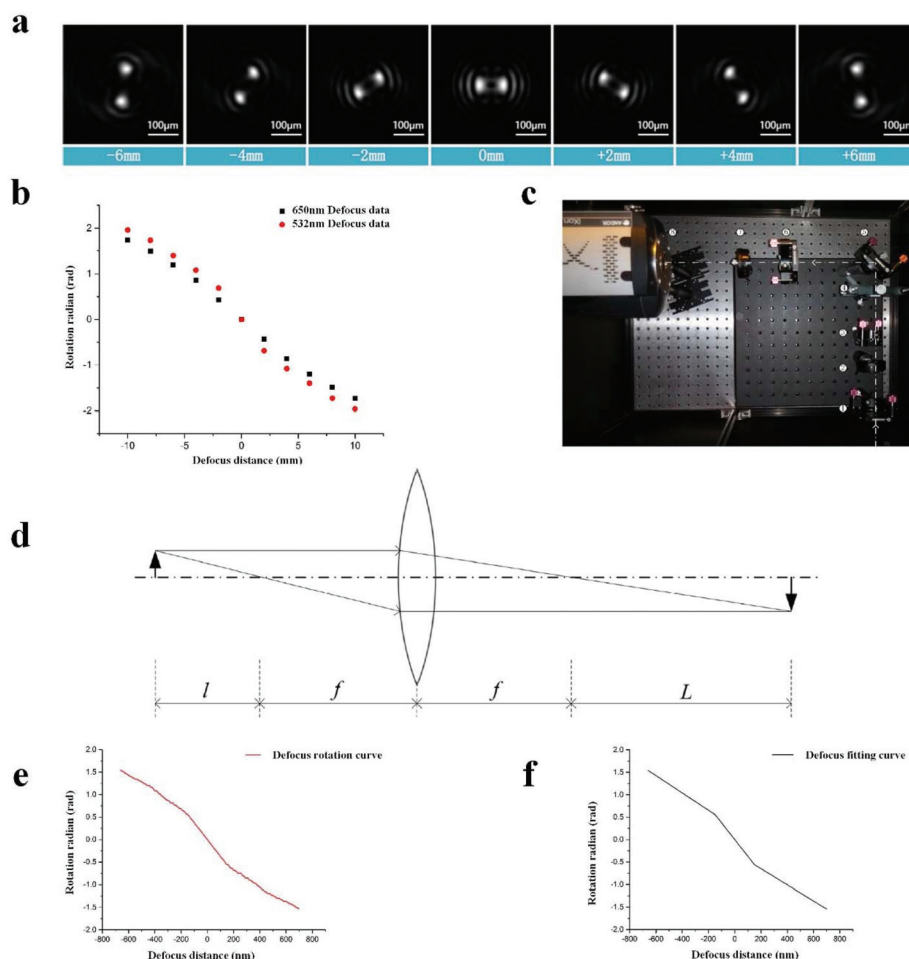
Fig. 6 Design of the quantum dot 3D tracking system. (a) Defocus images at a wavelength of 532 nm. (b) Comparison of defocus rotations at 650 nm and 532 nm. (c) 3D positioning system of quantum dot lens: ② aperture, ③ filter, ④ phase plate, ⑤ mirror, ⑥ lens, ⑦ aperture, and ⑧ camera. (d) Physical model of the eyepiece. (e) Defocus rotating curve. (f) Defocus fitting curve.

every 10 nm. The corresponding defocus imaging was then calculated and the rotation radian was extracted, yielding the relation curve shown in Fig. 6e.

This curve can be divided into three parts (Fig. 6e), where each part showing rotating arc approximately linear with respect to the defocus distance. Therefore, the curve was divided into three sections for fitting and the data are gathered in Table 2 and Fig. 6f.

The distance between imaging spots increased as the defocus distance increased. This was attributed to photosensitive cells of the camera used in the system with discrete arrays. Thus, the axial positioning resolution increased with the defocus distance. The simulations suggested that at the point source located on the focal plane of the object, the spacing of the imaging spot was estimated to be 78 μm. This was equivalent to 6-pixel spacing. The resolution of the corresponding rotating arc was $\frac{\pi}{6}$, and the resolution of axial positioning was 140 nm.

3.4. Application demonstration of the quantum 3D thermal imaging

Experiments were designed to locate quantum dots in liver cancer cells, measure temperature changes of quantum dots during the heating process, and verify the 3D temperature measurement capability of the micro–nanospace. The quantum dots were heated using a temperature controller.

An inverted fluorescence microscope was used to monitor the internalization of QDs into the cells and the images were captured and are shown in Fig. 7. From Fig. 7a, the image of the cells swallowed with QDs was acquired under white light mode. The plump morphology of the cells indicated that the cells were affected little by QD cytotoxicity and stayed in good

Table 2 Results of fitting

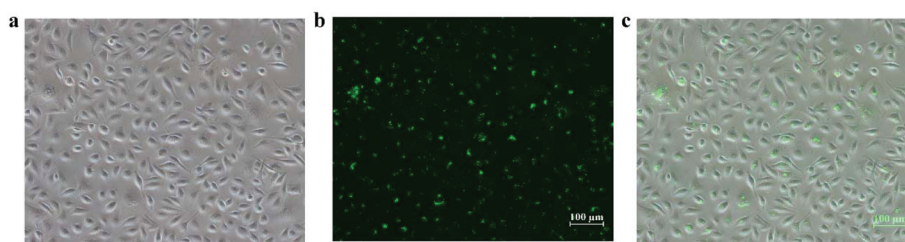| Defocus distance (nm)	Rotation radian (rad)	Fitting equation
−660 to −150	0.5586–1.544	$\theta = 0.2689 - 0.001932\Delta l$
−150–150	−0.5586–0.5586	$\theta = -0.003723\Delta l$
150–700	−1.544 to −0.5586	$\theta = -0.2896 - 0.001792\Delta l$

Fig. 7 Cell images after QD uptake under (a) white light and (b) ultraviolet wave band excitation light. (c) Combined picture of (a) and (b).
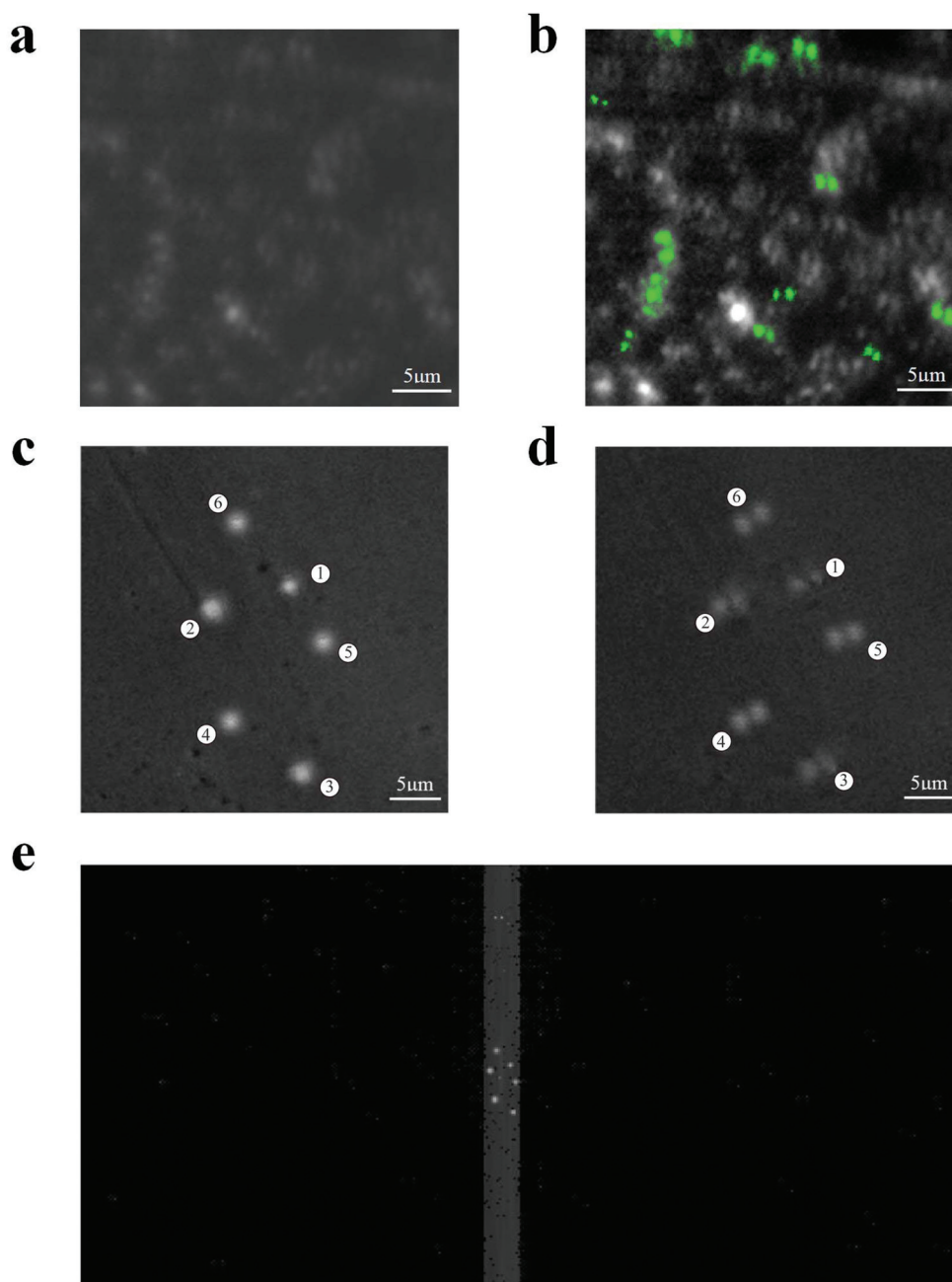

Fig. 8 Quantum dot imaging. (a) Quantum dot imaging in regions with higher concentrations – original acquisition imaging. (b) Quantum dot imaging in regions with higher concentrations – processed images. (c) Quantum dot imaging in regions with lower concentration without a phase plate, and (d) with lower concentration with a phase plate. (e) Quantum dot images obtained by using the spectrometer.

condition. Fig. 7b is the picture under fluorescence excitation mode. The picture shown in Fig. 7c is a combination of the aforementioned two pictures.

After image observation through the eyepiece, the position of the slide was adjusted to allow enough quantum dots within the field view with high fluorescence intensity. The working distance of the objective lens was adjusted to yield clear imaging. The camera was then employed to collect quantum dot imaging (Fig. 8a). The parameters of the thermal imaging system are as follows: the minimum exposure time of EMCCD is 0.01 s, and the electronic gain multiples range from 0 to 1000 times. Under considering the imaging clarity and noise interference, we choose 1 s as the exposure time, and the electron gain multiple is 25.

To distinguish the quantum dots from the background, the histogram equalization algorithm was adopted to improve the overall contrast of imaging. The influence of background noise was reduced by filtering the algorithm, and the quantum dots were marked as shown in Fig. 8b. Because of the high concen-

tration of quantum dots in the observed region, Fig. 7(b) marks only a few quantum dots in green (Fig. 8b).

To facilitate the experiment, the slide was moved and the eyepiece was used to observe and identify the region with dispersed quantum dots and strong fluorescence. Six quantum dots were identified in this region, taken as measurement objects and moved to the center of the field view (Fig. 8d). To further illustrate the imaging effect of positioning and tracking system on quantum dots, the phase plate was specifically taken out and imaging of quantum dots was recorded (Fig. 8c). The system double helix imaging capability of quantum dots was further confirmed.

The images of six quantum dots were processed with the image center as the origin of coordinates. The position of the pole bright spot in the double light spot was then extracted and connected. The midpoints were taken and their lateral position was calculated according to transverse calibration results. The axial position was calculated according to the inclination of the line and fitting equation shown in Table 2. The 3D positions of six quantum dots in the space were obtained and are listed in Table 3.

By adjusting the spectrometer slit, light outside the measured sub-point was excluded (Fig. 8e). Before spectral measurements, the spectrometer was first adjusted to spectral measurement mode and six regions were selected in the software, with included quantum dots. The spectral measurements were set to the automatic acquisition mode using 6 acquisitions, and a measurement interval of 60 seconds.

The temperature controller was set to 65 °C before starting to heat the quantum dots and the spectrum measurement

Table 3 Spatial position of quantum dots

Quantum dot no.	Rotation radian (rad)	Spatial location (X, Y, Z)
1	0.3672	(2.66 μm, −1.47 μm, −99 nm)
2	0.3883	(−4.80 μm, −2.62 μm, −104 nm)
3	0.4324	(3.89 μm, 13.02 μm, −116 nm)
4	0.3985	(−4.01 μm, 9.80 μm, −107 nm)
5	0.3424	(4.95 μm, −1.84 μm, −92 nm)
6	0.4612	(−3.02 μm, −6.40 μm, −124 nm)

Table 4 Temperature and fluorescence peak wavelengths of quantum dots during heating

| Time	QD① λ/nm	QD① T/°C	QD② λ/nm	QD② T/°C	QD③ λ/nm	QD③ T/°C	QD④ λ/nm	QD④ T/°C	QD⑤ λ/nm	QD⑤ T/°C	QD⑥ λ/nm	QD⑥ T/°C
0 s	534.67	23.85	543.60	23.47	543.93	25.40	543.72	24.26	543.70	24.10	543.67	23.94
60 s	544.14	26.60	543.70	24.00	544.43	28.31	544.28	27.53	544.19	27.00	544.12	26.58
120 s	544.58	29.14	543.70	24.00	544.74	30.16	544.68	29.86	544.61	29.45	544.46	28.60
180 s	544.83	30.68	544.43	28.30	545.31	33.45	545.00	31.78	545.07	32.20	544.75	30.25
240 s	545.30	33.52	544.81	30.54	545.31	33.45	545.19	32.90	545.30	33.51	545.22	33.06
300 s	545.58	35.02	546.13	38.25	545.45	34.30	545.68	35.76	545.44	34.35	545.66	35.65
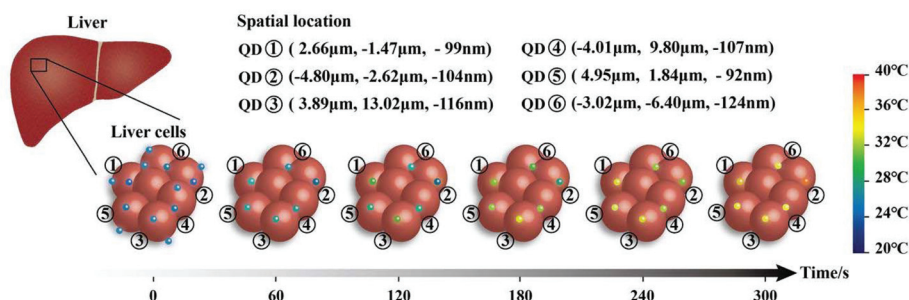
Fig. 9 Schematic diagram of quantum 3D thermal imaging of liver cells. The spatial location coordinates of the 3 quantum dots are (2.66 μm, −1.47 μm, −99 nm), (−4.80 μm, −2.62 μm, −104 nm), (3.89 μm, 13.02 μm, −116 nm), (−4.01 μm, 9.80 μm, −107 nm), (4.95 μm, −1.84 μm, −92 nm), and (−3.02 μm, −6.40 μm, −124 nm) respectively.

program automatically measures the quantum dot fluorescence.

Gaussian fitting was performed on the measured data, and temperatures of six quantum dots were obtained using eqn (2) and the results are listed in Table 4.

Overall, 3D localization and temperature measurement of quantum dots were experimentally achieved and the capability of the designed system was verified by 3D temperature. The realization of three-dimensional (3D) temperature distribution measurement at the micro–nanoscale would provide more advanced research methods and suitable technologies for biological based fields to clarify the relationship between life activities of the cells and heat. In turn, a study of the relationship between heat and metabolism of life would facilitate the control over progress of life activities through suitable generation of heat.

The quantum dots are injected into human tissues such as liver cells, and the location and temperature of the diseased cells can be measured, providing a new theoretical basis for accurate diagnosis of tumors at an early stage and helping in the discovery of new drugs. Based on the above data, we can imagine restructuring the quantum 3D thermal imaging of liver cancer cells as shown in Fig. 9.

4. Conclusions

The 3D temperature field gradient measurement method at the micro–nanoscale has profound scientific significance and good application prospects. The experiments showed the capability of the proposed theory and designed system with 3D thermal imaging for micro–nano space. Overall, the following conclusions could be drawn.

A new principle for 3D quantum thermal imaging at the nanometer level was proposed to solve the common problem of cell/particle temperature measurement and tracking. Real-time location/tracking and temperature measurement of quantum dots at the micro–nanoscale were achieved by the fluorescent effect of quantum dots and characteristics of the optical spot double helix. The proposed principle will provide new research ideas and advanced research tools for clarifying the phenomena related to life activities and dynamic properties of nanoparticles, expected to promote the innovation of materials science and life science.

A systematic design of a temperature measurement system of quantum dots, microscopic imaging system and quantum dot location system was proposed. A quantum 3D thermal imaging device was developed to establish nanoscale precision measurement and design theory system of the particle 3D temperature field distribution.

Conflicts of interest

There are no conflicts to declare.

Notes and references

1 J. Himmshagen, *Annu. Rev. Physiol.*, 1976, **38**, 315–351.
2 T.-H. Kim, K.-S. Cho, E. K. Lee, S. J. Lee, J. Chae, J. W. Kim, D. H. Kim, J.-Y. Kwon, G. Amaratunga, S. Y. Lee, B. L. Choi, Y. Kuk, J. M. Kim and K. Kim, *Nat. Photonics*, 2011, **5**, 176–182.
3 Y. Shirasaki, G. J. Supran, M. G. Bawendi and V. Bulovic, *Nat. Photonics*, 2013, **7**, 13–23.
4 J. K. Jaiswal, H. Mattoussi, J. M. Mauro and S. M. Simon, *Nat. Biotechnol.*, 2003, **21**, 47–51.
5 I. L. Medintz, H. T. Uyeda, E. R. Goldman and H. Mattoussi, *Nat. Mater.*, 2005, **4**, 435–446.
6 X. Michalet, F. F. Pinaud, L. A. Bentolila, J. M. Tsay, S. Doose, J. J. Li, G. Sundaresan, A. M. Wu, S. S. Gambhir and S. Weiss, *Science*, 2005, **307**, 538–544.
7 H. Monton, C. Parolo, A. Aranda-Ramos, A. Merkoci and C. Nogues, *Nanoscale*, 2015, **7**, 4097–4104.
8 G. Chen, F. Tian, Y. Zhang, Y. Zhang, C. Li and Q. Wang, *Adv. Funct. Mater.*, 2014, **24**, 2481–2488.
9 W. Wei, X. He and N. Ma, *Angew. Chem., Int. Ed.*, 2014, **53**, 5573–5577.
10 Y. Ma, M. Wang, W. Li, Z. Zhang, X. Zhang, T. Tan, X.-E. Zhang and Z. Cui, *Nat. Commun.*, 2017, **8**, DOI: 10.1038/ncomms15318.
11 P. A. S. Jorge, M. A. Martins, T. Trindade, J. L. Santos and F. Farahi, *Sensors*, 2007, **7**, 3489–3534.
12 J. M. Costa-Fernandez, R. Pereiro and A. Sanz-Medel, *TrAC, Trends Anal. Chem.*, 2006, **25**, 207–218.
13 L. Chen, G. Yang, P. Wu and C. Cai, *Biosens. Bioelectron.*, 2017, **96**, 294–299.
14 R. Liang, R. Tian, W. Shi, Z. Liu, D. Yan, M. Wei, D. G. Evans and X. Duan, *Chem. Commun.*, 2013, **49**, 969–971.
15 D. Pugh-Thomas, B. M. Walsh and M. C. Gupta, *Nanotechnology*, 2011, **22**, 185503.
16 D. Choudhury, D. Jaque, A. Rodenas, W. T. Ramsay, L. Paterson and A. K. Kar, *Lab Chip*, 2012, **12**, 2414–2420.
17 S. Li, K. Zhang, J. M. Yang, L. W. Lin and H. Yang, *Nano Lett.*, 2007, **7**, 3102–3105.
18 H. Sakaue, *Rev. Sci. Instrum.*, 2005, **76**, DOI: 10.1063/1.1988007.
19 H. Sakaue, A. Aikawa and Y. Iijima, *Sens. Actuators, B*, 2010, **150**, 569–573.
20 G. Kucsko, P. C. Maurer, N. Y. Yao, M. Kubo, H. J. Noh, P. K. Lo, H. Park and M. D. Lukin, *Nature*, 2013, **500**, 54–58.
21 Y. Li and B. Q. Li, *RSC Adv.*, 2014, **4**, 24612–24618.

22 E. Betzig, G. H. Patterson, R. Sougrat, O. W. Lindwasser, S. Olenych, J. S. Bonifacino, M. W. Davidson, J. Lippincott-Schwartz and H. F. Hess, *Science*, 2006, **313**, 1642–1645.

23 M. J. Rust, M. Bates and X. Zhuang, *Nat. Methods*, 2006, **3**, 793–795.

24 K. I. Willig, S. O. Rizzoli, V. Westphal, R. Jahn and S. W. Hell, *Nature*, 2006, **440**, 935–939.

25 S. M. King, S. Claire, R. I. Teixeira, A. N. Dosumu, A. J. Carrod, H. Dehghani, M. J. Hannon, A. D. Ward, R. Bicknell, S. W. Botchway, N. J. Hodges and Z. Pikramenou, *J. Am. Chem. Soc.*, 2018, **140**, 10242–10249.

26 H. Deschout, F. C. Zanacchi, M. Mlodzianoski, A. Diaspro, J. Bewersdorf, S. T. Hess and K. Braeckmans, *Nat. Methods*, 2014, **11**, 253–266.

27 L. Liu, J.-W. Liu, H. Wu, X.-N. Wang, R.-Q. Yu and J.-H. Jiang, *Anal. Chem.*, 2018, **90**, 1502–1505.

28 K. Ma, F. Zhang, N. Sayyadi, W. Chen, A. G. Anwer, A. Care, B. Xu, W. Tian, E. M. Goldys and G. Liu, *ACS Sens.*, 2018, **3**, 320–326.

29 A. von Diezmann, Y. Shechtman and W. E. Moerner, *Chem. Rev.*, 2017, **117**, 7244–7275.

30 H. Cang, C. M. Wong, C. S. Xu, A. H. Rizvi and H. Yang, *Appl. Phys. Lett.*, 2006, **88**, 223901–223903.

31 J. Fish and J. Scrimgeour, *Appl. Opt.*, 2015, **54**, 6360–6366.

32 N. P. Wells, G. A. Lessard and J. H. Werner, *Anal. Chem.*, 2008, **80**, 9830–9834.

33 G. Beaune, B. Dubertret, O. Clement, C. Vayssettes, V. Cabuil and C. Menager, *Angew. Chem., Int. Ed.*, 2007, **46**, 5421–5424.

34 R. Parthasarathy, *Nat. Methods*, 2012, **9**, 724–726.

35 M. Speidel, A. Jonas and E. L. Florin, *Opt. Lett.*, 2003, **28**, 69–71.

36 Z. Zhang and C.-H. Menq, *Appl. Opt.*, 2008, **47**, 2361–2370.

37 A. Dupont and D. C. Lamb, *Nanoscale*, 2011, **3**, 4532–4541.

38 A. Gahlmann, J. L. Ptacin, G. Grover, S. Quirin, A. R. von Diezmann, M. K. Lee, M. P. Backlund, L. Shapiro, R. Piestun and W. E. Moerner, *Nano Lett.*, 2013, **13**, 987–993.

39 M. A. Thompson, J. M. Casolari, M. Badieirostami, P. O. Brown and W. E. Moerner, *Proc. Natl. Acad. Sci. U. S. A.*, 2010, **107**, 17864–17871.

40 A. R. Carr, A. Ponjavic, S. Basu, J. McColl, A. M. Santos, S. Davis, E. D. Laue, D. Klenerman and S. F. Lee, *Biophys. J.*, 2017, **112**, 1444–1454.

41 P. Bon, J. Linares-Loyez, M. Feyeux, K. Alessandri, B. Lounis, P. Nassoy and L. Cognet, *Nat. Methods*, 2018, **15**(6), DOI: 10.1038/s41592-018-0005-3.

42 H. Bao, E. Wang and S. Dong, *Small*, 2006, **2**, 476–480.

43 N. Vyhnan and Y. Khalavka, *Luminescence*, 2014, **29**, 952–954.

44 X. Jiang, B. Q. Li, X. Qu, H. Yang and H. Liu, *J. Mater. Chem. B*, 2017, **5**, 8983–8990.

45 T. Rajh, O. I. Micic and A. J. Nozik, *J. Phys. Chem.*, 1993, **97**, 11999–12003.

46 M. Y. Gao, S. Kirstein, H. Mohwald, A. L. Rogach, A. Kornowski, A. Eychmuller and H. Weller, *J. Phys. Chem. B*, 1998, **102**, 8360–8363.